Average Current Control with Internal Model Control and Real-time Frequency Decoupling for Hybrid Energy Storage Systems in Microgrids

Alejandro Latorre, Wilmar Martinez, *Senior Member, IEEE,* and Camilo A. Cortes, *Senior Member, IEEE*

Abstract—Among hybrid energy storage systems (HESSs), battery-ultracapacitor systems in active topology use DC/DC power converters for their operations. HESSs are part of the solutions designed to improve the operation of power systems in different applications. In the residential microgrid applications, a multilevel control system is required to manage the available energy and interactions among the microgrid components. For this purpose, a rule-based power management system is designed, whose operation is validated in the simulation, and the performances of different controllers are compared to select the best strategy for the DC/DC converters. The average current control with internal model control and real-time frequency decoupling is proposed as the most suitable controller according to the contemplated performance parameters, allowing voltage regulation values close to 1%. The results are validated using real-time hardware-in-the-loop (HIL). These systems can be easily adjusted for other applications such as electric vehicles.

Index Terms—Internal model control, energy management system (EMS), hybrid energy storage system (HESS), microgrids, real-time frequency decoupling.

NOMENCLATURE

$\%e_{ts}$	Overshoot percentage
Δi	Current ripple
$\boldsymbol{A}, \boldsymbol{B}$, and $\boldsymbol{C}$	Matrices of state space model
C_1	Buck-mode output capacitor
C_2	Boost-mode output capacitor
C_{ic}	Current controller
$C_{ic,BB}$	Current controller for battery bank
$C_{ic,UCAP}$	Current controller for ultracapacitor (UCAP)
C_{IMC}	Compensator for internal model control (IMC)
$C_{vc,BB}$	Voltage controller for battery bank
$C_{vc,UCAP}$	Voltage controller for UCAP
D	Duty cycle
e_{ss}	Steady-state error
$F(s)$	IMC filter
$G_d(s)$	Disturbance transfer function
$G_p(s)$	Realistic model of plant
$\hat{G}_p$	Estimated mathematical model of plant
$G_{cl,A}, G_{cl,B}$	Closed-loop transfer functions of half-bridge converters A and B
G_{id}	Converter transfer function from current to duty cycle
I_{BB}	Current of battery bank
I_{DG}	Distributed generation current
i_L	Inductor current
i_{load}	Load current
i_{oA}	Output current of converter A
i_{oB}	Output current of converter B
i_{REF}	Current reference
I_{UCAP}	Current of UCAP
$\boldsymbol{K}$	Gain vector for state variables $\boldsymbol{x}$
$\boldsymbol{K}_i$	Gain vector for integral state variables $\boldsymbol{x}_i$
$\boldsymbol{K}_{BB}$	Gain vector for battery bank controller
$\boldsymbol{K}_{UCAP}$	Gain vector for UCAP controller
L	Inductor value
Me_{ts}	The maximum transient error
$Q(s)$	Function of IMC
$\boldsymbol{Q}$	Matrix of process noise covariance
R	Load resistance
$\boldsymbol{R}$	Matrix of measurement noise covariance
$r(t)$	Reference signal
$Ref_{FDC,A}, Ref_{FDC,B}$	Reference values for controllers in $G_{cl,A}$ and $G_{cl,B}$ using frequency decoupling
T_{vi}	Converter transfer function from voltage to current

A. Latorre is with the EMC-UN Research Group, Universidad Nacional de Colombia, Bogota, Colombia (e-mail: jalatorrec@unal.edu.co).

W. Martinez is with the KU Leuven, Campus Diepenbeek, EnergyVille 1-Genk, Belgium, Diepenbeek, Belgium (e-mail: wilmar.martinez@kuleuven.be).

C. A. Cortes (corresponding author) is with the EMC-UN Research Group, Universidad Nacional de Colombia, Bogota, Colombia (e-mail: caacortesgu@unal.edu.co).

$u(\cdot)$	Control law
v_H	Boost voltage
v_L	Buck voltage
v_o	Output voltage
V_{BUS}	DC bus voltage
V_{REF}	Voltage reference

I. INTRODUCTION

GLOBALLY, there has been a rapid development in using efficient technologies and systems with renewable energy resources [1]. Due to the nature of some renewable energy resources, the interaction between the traditional interconnected system and distributed energy resources (DERs) is complex [2], [3]. Reducing the complexity of this interaction is a key issue for the gradual development of the technologies that integrate renewable energy resources into the distribution system. Among the technologies, microgrids can respond in seconds to compensate for a deficit or surplus in a distribution system. Additionally, they can be designed to meet special requirements by users, e.g., reliability, efficiency, or uninterrupted power supply [4]-[6].

Modern microgrids use energy storage systems for different purposes like compensating the intermittent behavior of DERs. Energy storage systems are usually battery-based [5]-[7] and have operational limitations, especially in the applications with frequent pulsed load events such as residential microgrids and electric vehicles. However, recent research has shown that by combining different types of energy storage technologies such as battery-ultracapacitor systems, and the performance is improved in different ways by leveraging the operational benefits of each technology [8], [9]. These systems are known as hybrid energy storage systems (HESSs). For instance, batteries have high energy density but long response time, whereas ultracapacitors (UCAPs) have high power density and short response time. Therefore, in a conceptual HESS, batteries are usually installed to supply the average component of the power to the load, while UCAP supplies the transient component [10].

In order to achieve the desired characteristics in an HESS, it is required to select the proper topology for the system. Topologies can be classified as passive, semi-active, and active topologies [8], [9]. In the passive topology, the storage components are directly connected and the load exerts the control on the system. In the semi-active topology, a power converter is placed in the system and the control is partially exerted on this converter. In the active topology, it is required to install two power converters, one for each storage technology, thus increasing the control options for the system [8], [9].

The HESS in a parallel active topology couples the battery bank and the UCAP by using bi-directional DC/DC converters so that each storage component uses a dedicated converter and the sources are in parallel. At the opposite end of the storage components, DC/DC power converters are coupled to form a DC link, also called DC bus, to which the load is connected.

Storage components require bi-directional DC/DC power converters to facilitate power exchange. These converters obey the established operating rules that comprise the control systems. These control systems are commonly known as energy management systems (EMSs).

The performance of an HESS in an active topology is governed by the implemented control law [11], [12], which is part of the EMS. For the definition of the control law, it is usual to apply droop-based proportional-integral (PI) controllers. Reference [13] addresses the droop control to perform the frequency coordination using a virtual impedance for a DC microgrid. In this paper, a proportional control combined with low-pass filters (LPFs) and high-pass filters (HPFs) is applied to the battery controller and capacitor, respectively. The addressed strategy in [14] contains the undesirable steady-state error. Such error is also presented in [15] and [16].

In [14] and [17], the limitations of conventional droop control are identified for decentralized control in microgrids and power distribution between storage components. Additionally, the necessity of performing a dynamic power decoupling of different frequencies should be considered, which is not possible when only using a virtual resistor [14]. In order to solve the above limitations, it is proposed to extend the concept of virtual resistance towards the virtual capacitance by creating the concept of real-time frequency decoupling by means of extended droop control (EDC). In this case, the steady-state error is clearly reduced but it can be identified in pulsating load events and is only reduced when the load returns to its initial value.

As mentioned in [18], it is possible to manage external disturbances at the control level by implementing the internal model control (IMC), which is based on the internal model principle. The IMC structure includes an explicit robustness filter that is useful to manage modeling limitations and unmeasured disturbances [19]. Such characteristics make the IMC controller suitable for real-time plants in comparison with state space controllers and conventional proportional-integral-differential (PID) controller [18]. The tuning of the IMC controller is not very different from a conventional controller [19], but its potential is yet to be fully explored in power converter applications, given that it is not common to find implementations, especially when using coupled converters.

In the HESS applications, it is common to find control strategies that include the EMS within the control architecture, as evidenced in [15], [20], and [21]. In contrast, our previous research work [22] shows an EDC-based cascade control with no interdependence between the EMS and the control strategy.

Whether a microgrid is operating in grid-connected or island mode, the control objective may differ due to the changes in the operation conditions. The EMS must perform the required adjustments in response to such changes. The control objectives and operation conditions are sized according to the application. Therefore, the process variables are different from those expected in a manufacturing plant or in electric vehicles [23].

As mentioned above, HESSs are also used in electric vehi-

cles and plug-in hybrid vehicles. In [24], a semi-active topology is employed for electric vehicle applications with a coordination strategy, in which undesirable effects (pulsed load events) are not suppressed and Lithium-ion batteries are operating under a lot of stresses. Considering the differences of sizing and control objectives, the operating concepts are also compatible with residential microgrid applications. However, for the purpose of this paper, the sizing is made for residential microgrid applications, including low-power HESS and DERs.

References [10], [11], [25], and [26] about the HESS and its respective control system mainly focus on the electric vehicles. Therefore, the research about residential microgrids is important to identify and solve unreported problems.

This paper proposes an HESS in parallel active topology for residential applications. We evaluate different control techniques and propose a frequency decoupling cascade IMC as the controller for HESS in residential microgrid applications, due to its performance parameters regarding steady-state error and transient error. The validation of this study is performed by real-time simulation of an EMS that performs the control of the entire system.

The rest of this paper is divided into five sections. The system description and control architecture are presented in Section II. Section III outlines the performance parameters and different controllers to be tested. Section IV presents the evaluation of the control techniques used in simulation and the validation in hardware-in-the-loop (HIL) with an OPAL-RT. Finally, Section V presents the main conclusions of this paper.

II. System Description and Control Architecture

Figure 1 shows the HESS model in parallel active topology proposed in this paper, where the energy flows and the type of component in this system are identified in different colors.
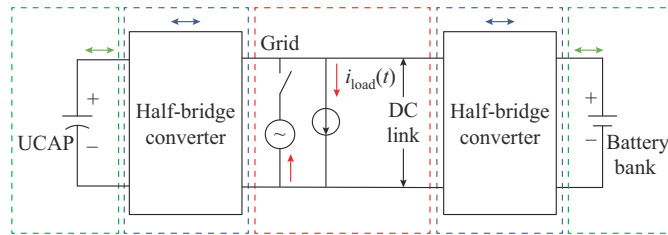

Fig. 1. HESS model in parallel active topology.

The components identified in green are the energy storage elements, where indirect control is applied. The components for direct control are identified in blue, and the components that interact with the system and whose dynamics are not controllable by the HESS are identified in orange.

In this paper, the indirect control is applied to the components that are dynamic but no control signal is applied directly on them. This is the case of the battery bank and the UCAP, which operate as a source or sink (charging) using bi-directional power converters, depending on the operation mode. Therefore, the energy flow is bi-directional.

The direct control is applied to bi-directional DC/DC power converters, where a pulse width modulation (PWM) control signal is exerted, which in turn responds to the control characteristic of each implemented controller.

The load and the distribution grid must be monitored in order to perform appropriate control actions and EMS-specific connections or disconnections. The load is modeled as a variable resistance, and the distribution grid is modeled as an approximate DC source by using a rectifier.

A. Half-bridge Converter

Power converters must properly harness the energy stored in both the UCAP and battery bank via the DC bus. This implies that the implemented converters and the control strategy must facilitate the interaction of the elements considering the characteristics of the system.

The bi-directional buck-boost converter or half-bridge converter is one of the most widely-used power converters [27]. Among other applications, it is used in the construction of hybrid vehicles. The half-bridge converter is a bi-directional converter, which can operate as boost or buck converter [28] according to the current flow direction. Moreover, it is easy to model, and can be conditioned to improve some characteristics [27], [28].

B. Converter Modelling

We use the average modelling by state variables described in [27] and [29] as the modelling strategy for the power converters in the same way as presented in [22]. Therefore, the models for the boost and buck models are presented in (1) and (2), respectively.

$$\begin{bmatrix} \dot{\tilde{i}}_L \\ \dot{\tilde{v}}_H \end{bmatrix} = \begin{bmatrix} 0 & \dfrac{1-\tilde{D}}{-L} \\ \dfrac{1-\tilde{D}}{C_2} & -\dfrac{1}{RC_2} \end{bmatrix} \begin{bmatrix} \tilde{i}_L \\ \tilde{v}_H \end{bmatrix} + \begin{bmatrix} \dfrac{V_L}{L(1-\tilde{D})} \\ \dfrac{-V_L}{RC_2(1-\tilde{D})^2} \end{bmatrix} \tilde{D} \quad (1)$$

$$\begin{bmatrix} \dot{\tilde{i}}_L \\ \dot{\tilde{v}}_L \end{bmatrix} = \begin{bmatrix} 0 & -\dfrac{1}{L} \\ \dfrac{1}{C_1} & -\dfrac{1}{RC_1} \end{bmatrix} \begin{bmatrix} \tilde{i}_L \\ \tilde{v}_L \end{bmatrix} + \begin{bmatrix} \dfrac{V_H}{L} \\ 0 \end{bmatrix} \tilde{D} \quad (2)$$

where $\widetilde{(\cdot)}$ represents the state variables.

C. Control Architecture

The strategy used in each operating mode, i.e., island or grid-connected mode, must control the voltage and current of the power converters according to the performance and safety parameters.

Among the basic operating characteristics of HESS in residential microgrid applications, the response to sudden changes in the load and/or generation is identified as a critical need. In that case, it is desirable that the battery bank supplies the energy associated with the average current, while the UCAP delivers the power required for the transient states and the dynamic component of the aggregated load-generation. Figure 2 shows the general architecture designed to meet the above functional requirements.
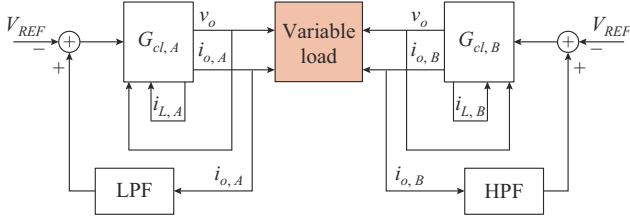
Fig. 2. General control architecture.

Figure 2 distinguishes two main feedback loops. The internal loop contains the feedback of control variables i_L and v_o for current and voltage regulation, as shown in [28]. The external loop corresponds to the real-time frequency decoupling loop.

For the denoted system $G_{cl,A}$, the reference signal $r(t)$ is given by:

$$Ref_{FDC,A} = r(t) - |LPF| i_{o,A} \tag{3}$$

For the denoted system $G_{cl,B}$, the reference signal $r(t)$ is given by:

$$Ref_{FDC,B} = r(t) - |HPF| i_{o,B} \tag{4}$$

The measurement of the output current in each converter is required for the operation of frequency decoupling loop. The filter in this loop is working as a virtual impedance, thus we obtain the real-time frequency decoupling loop by subtracting the reference value from the product of the virtual impedance and the output current.

D. EMS

From the desired control objectives, we extract the operating rules of the EMS so that we can easily identify the required actions in the possible scenarios. The EMS also includes converter controllers as part of the system. This approach combines the classic droop control with a unified controller according to [9].

In the operating rules of the EMS, we consider several variables such as the state of charge (SOC) of the battery bank, the voltage of UCAP, the state of the distribution grid, and the generation current.

Control actions for the battery bank include hard charge, soft charge, discharge, connection, and disconnection. The UCAP uses the same control actions, expecting that the hard and soft charge actions are replaced by normal charge actions.

The operating rules applicable to the distribution grid include only connection and disconnection in relation to the reference voltage. The cases of DERs include connection and disconnection commands, when the generation current I_{DG} is greater than zero. Further details about EMS rules can be found in [22].

III. CONTROL TECHNIQUES

The comparison of different control strategies and their performance evaluation are important to select the most appropriate option for the validation process. Compared with the controllers in the grid-connected mode, we emphasize controllers in the island mode due to the general interest they represent in the application.

A. Performance Parameters

There are multiple indicators evaluating the performance of a control system. In [30], the steady-state error is proposed as the single performance evaluation parameter. However, it is necessary to use additional indicators in HESS applications such as the overshoot percentage and the maximum transient error, as stated in [31]

Consequently, the following performance evaluation parameters are used in this paper, i.e., the steady-state error e_{ss}, the maximum transient error $M_{e_{ts}}$, the overshoot percentage $\%e_{ts}$, set-point tracking, and load response.

B. Vectorial PI Control

Vectorial PI (VPI) control is considered as an extension of the state feedback control, which is widely studied and disseminated. The concept of integral action in PI control is extended to compensate the limitations of robustness and steady-state error in the state feedback control. When considering the error integral as a state variable, the aforementioned virtues are incorporated into the control technique [32]. As a result, the system is presented as:

$$\begin{bmatrix} \dot{x} \\ \dot{x}_i \end{bmatrix} = \begin{bmatrix} A - BK & -BK_i \\ C & 0 \end{bmatrix} \begin{bmatrix} x \\ x_i \end{bmatrix} + \begin{bmatrix} B \\ -1 \end{bmatrix} r(t) \tag{5}$$

$$x = \begin{cases} \begin{bmatrix} i_L \\ v_H \end{bmatrix} & \text{boost mode} \\ \begin{bmatrix} i_L \\ v_L \end{bmatrix} & \text{buck mode} \end{cases} \tag{6}$$

Both vectors K and K_i can be obtained by pole placing methods or following the Ackermann formula [32], [33]. The control law for this controller is given by:

$$u(t) = r(t) - Kx - K_i x_i \tag{7}$$

Using the pole placing method, we obtain the gain vectors of the battery bank and UCAP in VPI control, i.e., $K_{BB,VPI}$ and $K_{UCAP,VPI}$, respectively, as shown in (8).

$$\begin{cases} K_{BB,VPI} = \begin{bmatrix} 0.0110 & -0.0016 & -0.0470 \end{bmatrix} \\ K_{UCAP,VPI} = \begin{bmatrix} 0.4368 & 0.1714 & -49.05 \end{bmatrix} \end{cases} \tag{8}$$

C. Lineal Quadratic Integral Control

As an alternative to the pole placing method, an optimization method called linear quadratic regulator (LQR) or quadratic optimal regulator is proposed in [33].

As one of the aforementioned VPI control, the linear quadratic integral (LQI) control is an extension of the LQR control, which has limitations of steady-state error. However, unlike the state feedback control, it has no robustness limitations.

For the LQI controller, it is valid to use the same block diagram applied to VPI control, since the same strategy is used to enhance the system and add a virtual state variable x_i to obtain the control law presented in (7).

In order to obtain the feedback gain vector, it is required to minimize the cost function in (9).

$$J = \int_0^\infty (x^T Q x + u^T R u) dt \tag{9}$$

where $Q \geq 0$ is a semi-defined positive symmetric matrix, whose rank is equal to that of the process noise covariance matrix A; and $R > 0$ is a definite positive symmetric matrix, called measurement noise covariance matrix [34]. The matrices Q and R are weight matrices that include the design criteria [33]. The control law in (7) is adapted to the optimization problem using (10).

$$u(t) = -R^{-1} B^T P x(t) \tag{10}$$

In (10), the matrix P has a rank of n and satisfies the algebraic Riccati equation:

$$PA + A^T P - PBR^{-1} B^T P + Q \tag{11}$$

By obtaining the value of P, it is possible to calculate the matrix K that meets the established conditions:

$$K = R^{-1} BP \tag{12}$$

There are multiple alternatives for selecting the weights assigned to the matrices Q and R that are part of the LQI control. In [33] and [35], the test and error strategies are presented, while Bryson's rule is used in [34] to set initial parameters and perform a matrix adjustment process.

According to [34], Bryson's rule for the matrix Q with a rank of j states that the main diagonal element Q_{jj} is given by:

$$Q_{jj} = \frac{1}{\max(X_j^2)} \tag{13}$$

where $\max(\cdot)$ stands for the maximum acceptable value. Similarly, Bryson's rule for the matrix R with a rank of k affirms that the main diagonal element R_{kk} are obtained by:

$$R_{kk} = \frac{1}{\max(u_t^2)} \tag{14}$$

When applying Bryson's rule for the weight matrices of the battery bank and the UCAP, the required gain vectors $K_{BB,LQI}$ and $K_{UCAP,LQI}$ are obtained by including the results into a computational tool based on MATLAB.

$$\begin{cases} K_{BB,LQI} = [\,0.11630 \quad 0.0132 \quad -4.4721\,] \\ K_{UCAP,LQI} = [\,0.0572 \quad 0.0473 \quad -10.9545\,] \end{cases} \tag{15}$$

The LQI controller with integral action is achieved by replacing the obtained gains into (7).

D. ACC

The cascade double-loop voltage and current control or average current control (ACC) is widely used in power electronics applications, which is also considered in this case based on the PID controller tuning for both voltage control and current control. The control architecture is discussed in our previous works [22], and in [12] and [17].

The design criterion in [12] and [28] requires that the current controller must have a bandwidth of approximately 10% of the converter switching frequency. We present the transfer functions of the current controllers $C_{ic,BB}$ and $C_{ic,UCAP}$ in (16).

$$\begin{cases} C_{ic,BB} = \dfrac{313.5s^2 + 3.663 \times 10^5 s + 1.07 \times 10^8}{s^2 + 3.427 \times 10^4 s} \\ C_{ic,UCAP} = \dfrac{18.48s^2 + 6.132 \times 10^4 s + 5.05 \times 10^7}{s^2 + 1.977 \times 10^5 s} \end{cases} \tag{16}$$

The criterion of voltage controller defined in [28] requires a bandwidth of approximately 10% of the current controller bandwidth. We present the transfer functions of the voltage controllers $C_{vc,BB}$ and $C_{vc,UCAP}$ in (17).

$$\begin{cases} C_{vc,BB} = \dfrac{544.4}{s} \\ C_{vc,UCAP} = \dfrac{428.38}{s} \end{cases} \tag{17}$$

E. ACC with IMC

IMC is considered as a predictive control method [28] that allows canceling delays induced by the plant and thus achieves a wider bandwidth in the closed loop, while the behavior of the system is stable.

The IMC principle applied to control theory, as stated in [36], introduces an explicit model of the plant into the control architecture, as expressed in (18).

$$C_{IMC} = \frac{F(s)Q(s)}{1 - F(s)Q(s)\hat{G}_p(s)} \tag{18}$$

Equation (18) is composed of the estimated mathematical model of the plant $\hat{G}_p(s)$ calculated from the realistic model of the plant $G_p(s)$, a stable IMC function $Q(s)$ incorporating the corresponding controller, and the IMC filter $F(s)$ to improve the robustness with respect to the modelling error [37].

Depending on the control objectives and the system to be controlled, different control strategies can be applied to obtain a proper and stable function $Q(s)$ such as PID control, LQR, coprime factorization, etc. [37].

Furthermore, [38] presents an architecture for a two-degree controller, whose implementation would be excessively complex. Reference [39] employs the IMC for a simple buck converter. The approach in [40] includes robust control techniques for an IMC controller, which is also highly complex. Therefore, we discard such strategies.

In our previous research work, we have executed test cases containing two cascading IMC compensators, following the architecture of the ACC. The results show that the current controller suppresses the effect of the real-time frequency decoupling loop, and therefore, we also discard these test cases. We choose to replace the IMC controller with the controller incorporated in the current loop for ACC.

In this way, we obtain a cascaded controller with a PID current control and IMC voltage control in a simple architecture. The block diagram of the proposed controller is shown in Fig. 3. In this diagram, the transfer function $C_{ic}(s)$ is the current controller as used in the ACC, and $G_{id}(s)$ is the model transforming the current to duty cycle.
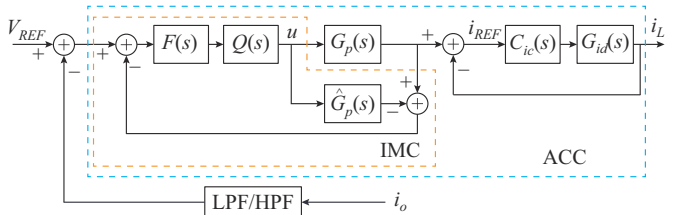
Fig. 3.   Block diagram of proposed controller.

For the estimated model, we use the closed-loop transfer function with current control, and therefore, $\hat{G}_p(s) = T_{vi}(s)$. Moreover, for the battery bank voltage controller, the voltage controller is given as:

$$C_{vc,BB} = \frac{\alpha s^3 + \beta s^2 + \delta s + \zeta}{s^3 + \rho s^2 + \sigma s + \xi} \tag{19}$$

where $\alpha = 1.97 \times 10^{-3}$; $\beta = 97.11$; $\delta = 3.17 \times 10^6$; $\zeta = 877.2 \times 10^6$; $\rho = 14.56 \times 10^3$; $\sigma = 15.14 \times 10^6$; and $\xi = 4.05 \times 10^9$.

For the UCAP controller, the voltage controller is given by:

$$C_{vc,UCAP} = \frac{\gamma s^4 + \alpha s^3 + \beta s^2 + \delta s + \zeta}{s^4 + \phi s^3 + \rho s^2 + \sigma s + \xi} \tag{20}$$

where $\gamma = 18.89 \times 10^{-3}$; $\alpha = 9405$; $\beta = 1.25 \times 10^9$; $\delta = 36.6 \times 10^{12}$; $\zeta = 2.07 \times 10^{15}$; $\phi = 440.8 \times 10^3$; $\rho = 10.13 \times 10^9$; $\sigma = 24.79 \times 10^{12}$; and $\xi = 15.1 \times 10^{15}$.

IV. Control Performance Assessment and Validation

For the different control techniques, we run simulations in Simulink by using the same test scenario. The models for each controller used in this stage are available in [41]. Table I summarizes the power converter parameters used in the HESS for this section.

TABLE I
SUMMARY OF PARAMETERS FOR HALF-BRIDGE CONVERTERS

Converter	Rated power (kW)	Boost voltage (V)	Buck voltage (V)	Switching frequency (kHz)	Inductance (mH)	Low-side capacitor	High-side capacitor
Battery bank converter	5	360	210	10	5.2	100 mF	262.7 μF
UCAP converter	5	360	184	30	4.6	390 μF+20 F	1.29 mF

The unipolar voltage of DC bus is 360 V and it is coupled to a variable pulsating load with different current levels. The rated voltage and capacity of battery bank are 160 V and 6912 Wh, respectively, and the rated voltage and capacity of UCAP are 230 V and 20 F, respectively, and equivalent series resistance is 340 mΩ.

Based on the simulation results, we carry out the performance evaluation considering the parameters indicated in Section III-A and apply them to the voltage of DC bus. For the battery bank current, we use qualitative parameters.

A. Voltage of DC Bus

Table II shows the performance parameters with different controllers. Additionally, we compare the voltage of DC bus V_{BUS} with different controllers in Fig. 4. All results in Table II can be replicated based on [41].

TABLE II
PERFORMANCE PARAMETERS WITH DIFFERENT CONTROLLERS IN ISLAND MODE

Controller	$e_{ss,av}$ (mV)	$Me_{ts}^{(+)}$ (V)	$Me_{ts}^{(-)}$ (V)	$\%e_{ts}^{(+)}$ (%)	$\%e_{ts}^{(-)}$ (%)	Set-point tracking	Load response
VPI	163.5	4.2	4.2	1.16	1.16	Regular	Suitable
LQI	88.1	2.3	1.8	0.64	0.50	Suitable	Suitable
ACC	30.4	2.4	1.8	0.66	0.50	Suitable	Suitable
IMC	22.6	2.0	1.6	0.55	0.44	Suitable	Suitable

Note: the superscripts "+" and "−" represent the positive and negative errors, respectively.

For the steady-state error, the mean value of the acquired signal is compared with the set-point value. The maximum overshoots are measured from the local maximum and minimum values in the worst case. The overshoot percentages are based on the normalization of the difference between the maximum and minimum values and the reference value, while the set-point tracking is qualitatively assessed from the steady-state error and transient error.


Fig. 4.   Voltage of DC bus with different controllers.

Note that in Table II that the highest steady-state error $e_{ss,av}$ is obtained with the VPI control (163.5 mV) and the lowest one is obtained with the IMC (22.6 mV).

In the case of the maximum positive and negative transient errors $Me_{ts}^{(+)}$ and $Me_{ts}^{(-)}$, the VPI control has the highest values (4.2 V), while the IMC presents the lowest positive and negative errors (2 V and 1.6 V, respectively). In the same way, the overshoot percentage of the VPI control is the highest at 1.16%, while the IMC has a maximum positive excess of 0.55% and a maximum negative excess of 0.44%. Therefore, in the transient state, the IMC shows a superior performance.

For all controllers, except for the VPI control, the set-point tracking is rated as suitable, as there is a tendency to quickly reduce the transient error. In the case of the VPI control, there is a tendency to reduce the error. However, the response is not adequate in the case of abrupt load changes since an reduction close to the set-point value is not achieved.

1) Disturbance Response

In addition to the aforementioned tests, we carry out a

case scenario to show the response of controllers to voltage disturbances. The disturbances are included in the controller from dy, where y is the output signal, which is the output voltage v_o in this case. The disturbance signal is included in the system in the form of (21), where the coefficient is used to amplify or attenuate the disturbances magnitude for test purposes.

$$G_d(s) = 4\frac{1}{s+1} \qquad (21)$$

We define the coefficient as a constrain for the ACC in (21), given that using a higher value makes the response unstable. The simulation results for this case are presented in Fig. 5, from which we can identify that the VPI and LQI have similar responses, and the waveform of VPI is consistent with the undisturbed case. Moreover, the IMC and the ACC also have similar responses; however, the ACC response shows marginal stability at the local maximum and minimum values, which is undesirable for dynamic stability.
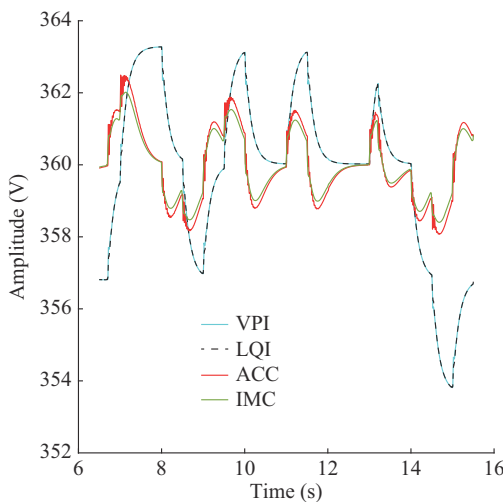
Fig. 5. Voltage disturbance response with different controllers.

The IMC response in Fig. 5 has no difference compared with that in Fig. 4, which is the expected result considering the internal model principle. From Table III, we summary the performance parameters with different controllers in island mode considering voltage disturbances. The result has the same parameters with the IMC in the undisturbed case, which indicates that IMC is less prone to instabilities in a more realistic disturbed scenario, while the other controllers present a reduced performance. All results in Table III can be replicated based on [41].

TABLE III
PERFORMANCE PARAMETERS WITH CONTROLLERS IN ISLAND MODE
CONSIDERING VOLTAGE DISTURBANCES

Control-ler	$e_{ss,av}$ (mV)	$Me_{ts}^{(+)}$ (V)	$Me_{ts}^{(-)}$ (V)	$\%e_{ts}^{(+)}$ (%)	$\%e_{ts}^{(-)}$ (%)	Set-point tracking	Load response
VPI	1.09	5.1	6.2	1.41	1.72	Regular	Regular
LQI	771.00	3.3	6.2	0.91	1.72	Regular	Regular
ACC	28.20	2.5	1.9	0.69	0.52	Suitable	Suitable
IMC	22.60	2.0	1.6	0.55	0.44	Suitable	Suitable

2) Simulation Results in Island Mode

Considering that the IMC has the best performance according to the performance evaluation parameters both with and without voltage disturbances, we run additional simulations for this controller. The results are shown in Fig. 6, placing the steady-state voltage error using two different scales, the pulsating load current profile for the test cases and the current waveforms of the storage components.
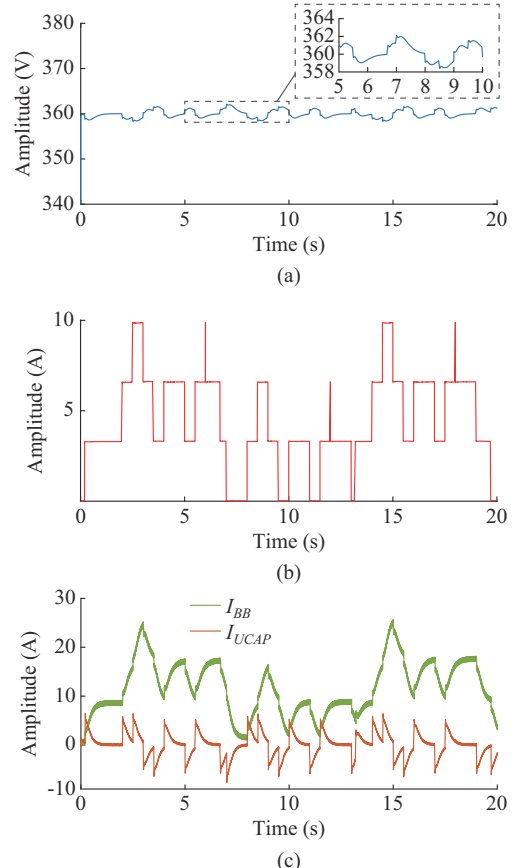
Fig. 6. Simulation of an HESS in island mode using IMC. (a) V_{BUS}. (b) I_{load}. (c) I_{BB} and I_{UCAP}.

The HESS response to the load with different controllers is considered adequate since we identify that all the load is supplied during the simulation interval. The waveform differences in different cases are practically imperceptible, so there is no distinguishing factor. In the case of pulsating load events at $t = 6$ s, 12 s, and 18 s, it can be observed that there is a load shedding. These events are short pulses that quickly return to the initial value, thus the HESS dynamics is required not to be so fast.

B. Current of Battery Bank

Although the current of battery bank I_{BB} is not covered within the performance parameters, it is important to analyze it because the battery is the main storage component of the HESS and some of its characteristics, e.g., shelf life and operating temperature, can be affected by the change of controller. Figure 7 shows the comparison of I_{BB} with different controllers.
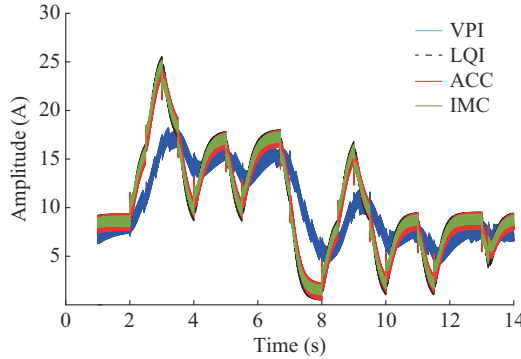
Fig. 7.   Current of battery bank with different controllers.

The VPI controller has an average current of $I_{BB,av} = 11.29$ A with a maximum value of $I_{BB,max} = 18.3$ A and a behavior susceptible to a disturbance, which attributes to not only the load changes but also the adjustments made by the controller. With the VPI controller, the current ripple is $\Delta i \approx 1.7$ A.

The LQI controller presents an average current of $I_{BB,av} = 11.55$ A with a maximum value of $I_{BB,max} = 26.02$ A and a behavior less susceptible to a disturbance, which is different from abrupt load changes. During the simulation, the load change may cause short leaps with an average amplitude of approximately 1 A. In those leaps, there are positive and negative overshoots with an average amplitude of approximately 0.41 A. In this case, the current ripple is $\Delta i \approx 1.71$ A.

The result of ACC is similar to that of the LQI control, but there are some differences in terms of amplitude. For the battery bank, the ACC has an average value of $I_{BB,av} = 11.48$ A and a maximum value of $I_{BB,max} = 25.5$ A. However, in this case, the overshoots have an average amplitude of approximately 1.38 A and there is a current ripple of $\Delta i \approx 1.72$ A.

The IMC has a behavior with subtle differences compared with ACC. First, the average current is $I_{BB,av} = 11.51$ A and the maximum is $I_{BB,max} = 25.67$ A (the largest of the studied cases). Second, the current leaps have no overshoot and an approximate average amplitude of 1.94 A. Finally, the current ripple is $\Delta i \approx 1.01$ A.

C. Assessment of Controllers

We compare different controllers by applying the performance parameters to the DC bus voltage. The overall assessment is carried out by assigning a standard rating of 1 to 10 to each component, depending on the mean value and the standard deviation. The values obtained are reported in Table IV.

TABLE IV
ASSESSMENT OF VOLTAGE CHARACTERISTICS

Parameter	e_{ss} (mV)	$Me_{ts}^{(+)}$ (V)	$Me_{ts}^{(-)}$ (V)	$\%e_{ts}^{(+)}$ (%)	$\%e_{ts}^{(-)}$ (%)
Mean value	76.4	2.72	2.35	0.75	0.65
Standard deviation	65.1	0.99	1.23	0.27	0.34

Figure 8 shows the assessment of performance parameters with different controllers.
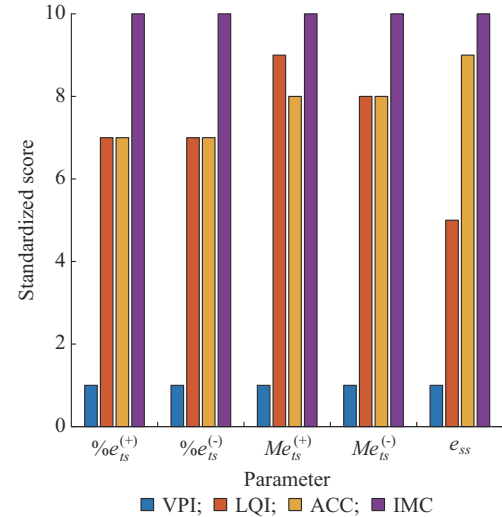

Fig. 8.   Assessment of performance parameters with different controllers.

According to Fig. 8, the ACC with IMC outperforms other controllers in all evaluation parameters. Additionally, the IMC is less prone to the effect of external disturbances and mathematical assumptions during modeling and tuning, which is convenient for real-time implementations.

Since the IMC performance is notable in all categories, we use this technique in the implementation process in HIL.

D. Result Validation

For the implementation of HESS-EMS, we develope different test cases for real-time simulation on a platform of OPAL-RT Technologie for HIL OPAL-RT OP4510. The signals generated by the OPAL-RT are acquired through a terminal block array and a four-channel Tektronix TBS 2000 (100 MHz/1 GS/s) oscilloscope, and processed via a PC, as depicted in Fig. 9. The characteristics of HESS at this stage are summarized in Table V.
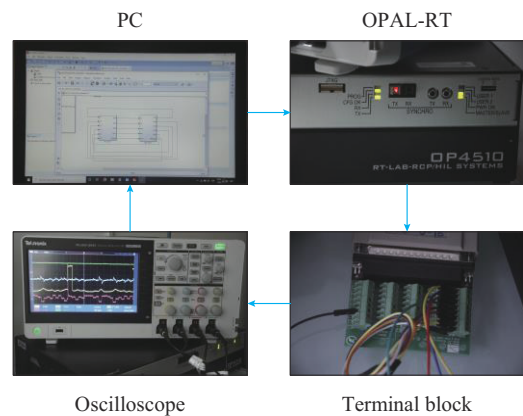

Fig. 9.   HIL validation setup.

The EMS uses the same rules as mentioned in Section II and detailed in [22]. We include the ACC with the previously assessed IMC. In this case, the load value is constant or manually changed and the pulsed events are introduced by pseudo-random generated changes in time and magnitude, and is applied to the system as a DER.

TABLE V
SUMMARY OF PARAMETERS OF HALF-BRIDGE CONVERTERS FOR HIL IMPLEMENTATION

Converter	Rated power (kW)	Boost voltage (V)	Buck voltage (V)	Switching frequency (kHz)	Inductance (mH)	Low-side capacitor (mF)	High-side capacitor
Battery bank converter	5	360	170	4	6	1	1 mF
UCAP converter	5	360	184	12	3	100	180 µF

Figure 10 shows the single-line diagram of the HESS-EMS implemented in the OPAL-RT. The reference directions of current flow are identified for the interpretation of the results presented in the subsequent sections.
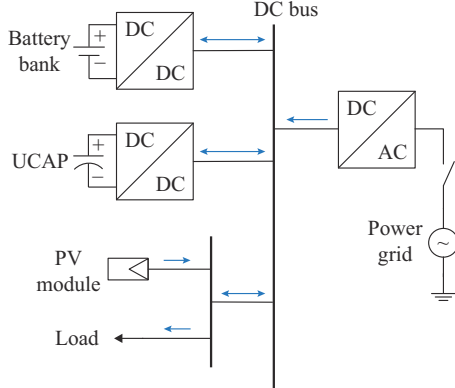
Fig. 10. Single-line diagram of HESS-EMS for implementation in OPAL-RT.

According to the single-line diagram in Fig. 10, the storage components require bi-directional current flow and there is a positive sign when energy consumption occurs. In the test cases, the current flow from the power grid to DC bus is unidirectional.

If the current difference between the PV module and the load is greater than zero (if there is a charging condition), the current flow to the DC bus must be positive. Consequently, the current flow to the DC bus will be negative when there is a consumption condition.

1) Operation in Island Mode with $I_{load} < I_{DG}$

Figure 11 presents the real-time simulation for the HESS-EMS in the island mode with DER, a fixed load of 800 W, an initial state of charge (SOC) of the battery bank at 80%, and the initial voltage of 189 V in the UCAP.

The results of I_{BB} and I_{UCAP} are obtained from the real-time frequency decoupling and the difference between I_{DG} and I_{load}. The amplitude of I_{BB} changes gently as the generation current increases or decreases, while the amplitude of I_{UCAP} has abrupt changes.

Moreover, the response of DC bus voltage V_{BUS} is remarkable, since the voltage is maintained with a steady-state error close to 1 V ($\approx 0.27\%$) and a maximum transient state error of 2.1 V ($\approx 0.58\%$) during an abrupt change in the DER current.

2) Operation in Island Mode with $I_{load} > I_{DG}$

The initial SOC of battery bank is 80%, the UCAP voltage is 189 V, and the initial load is 800 W. As shown in Fig. 12, after approximately two minutes of operation, a load change reaches 2500 W, which is maintained during the remaining testing time.
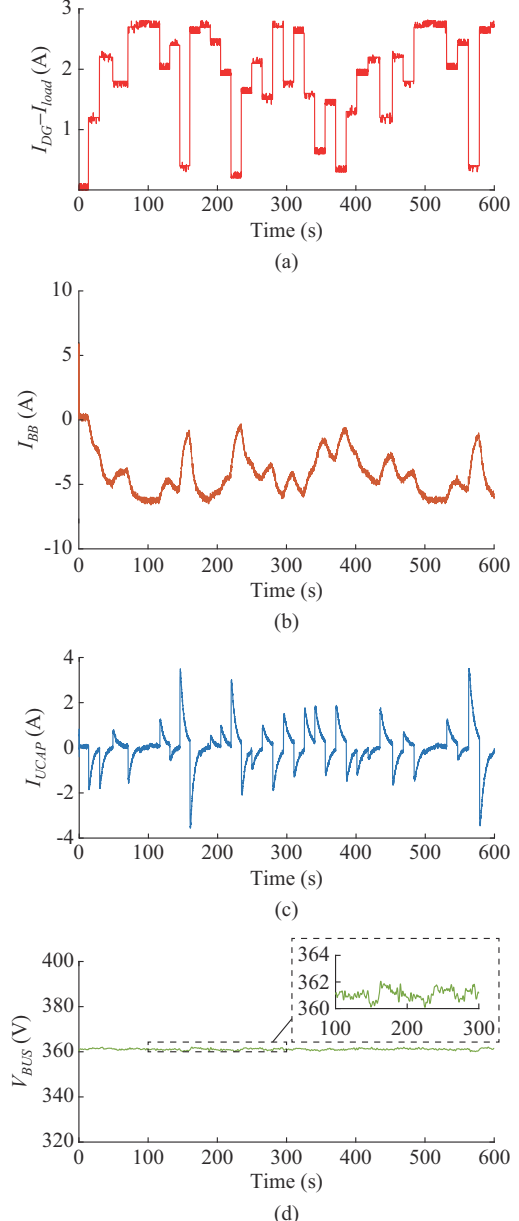

Fig. 11. OPAL-RT implementation results for normal operation in island mode with $I_{load} < I_{DG}$. (a) $I_{DG} - I_{load}$. (b) I_{BB}. (c) I_{UCAP}. (d) V_{BUS}.

As shown in Fig. 12, the abrupt load changes at about $t = 120$ s. After that, the current $I_{DG} - I_{load}$ becomes negative. As mentioned above, this implies that the load to be supplied is greater than the DER current.

For I_{BB}, the load change has a transient with rising time in about 20 s. The subsequent variations caused by the changes in generation have similar rising time, which would contribute to increase the expected lifetime of the battery.
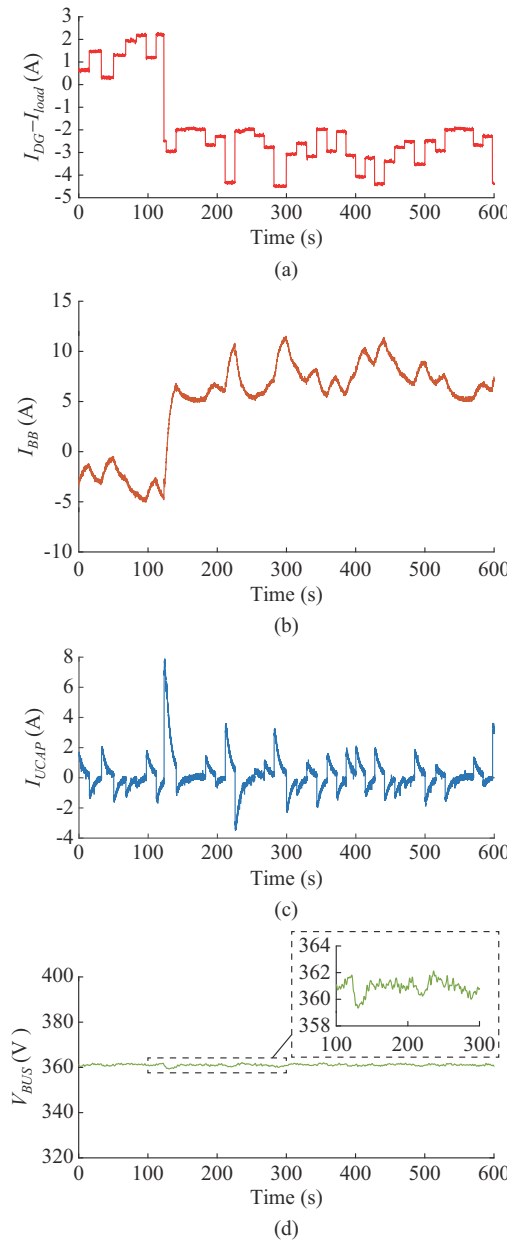
Fig. 12.   OPAL-RT implementation results for normal operation in island mode with $I_{load} > I_{DG}$. (a) $I_{DG} - I_{load}$. (b) I_{BB}. (c) I_{UCAP}. and (d) V_{BUS}.

Additionally, the DC bus voltage V_{BUS} is stable throughout the test, with an approximate steady-state error of 0.3% and a maximum overshoot of about 0.7% during the load change.

E. Comparison of Performance Parameters

Although the load profiles are different for the simulation processes and the implementation in HIL, we make a comparison considering the performance parameters for the voltage of the DC bus. This comparison covers the IMC controller test case and the HIL test case for island mode operation with $I_{load} > I_{DG}$. The data are listed in Table VI.

From the performance parameters in Table VI, it is clear that the deviation between the simulation and HIL implementation is small in all parameters, which validates the simulation results.

The steady-state error and its corresponding percentage value show a noticeable difference, which is the worst case for the HIL implementation. However, the value of e_{ss} in HIL is considered more realistic and a 0.3% error for a 360 V DC bus is negligible. This means that the proposed controller has a good steady-state performance.

The maximum positive overshoot and its corresponding percentage value exhibit a difference of 0.25%, which is in favor of the HIL implementation. The maximum negative overshoot and its corresponding percentage value differ at 0.14%, which is in detriment of the HIL implementation. The result is remarkable for the proposed controller and the process carried out, which also has a good performance in the transient state both for the positive and negative load changes at different amplitudes.

Load response and set-point tracking parameters are analyzed with a more comprehensive approach, because these indicators exhibit a consistent behavior in the different HIL test cases. The set-point tracking indicator validates that the operation is adequate, since both the steady-state and transient errors are low. Moreover, the load response also confirms that the behavior of the IMC with real-time frequency decoupling allows the system to supply the load with pulsed current in island mode.

TABLE VI
COMPARISON OF PERFORMANCE PARAMETERS FOR SIMULATION AND HIL

Parameter	e_{ss} (V)	% e_{ss} (%)	$Me_{ts}^{(+)}$ (V)	$Me_{ts}^{(-)}$ (V)	%$e_{ts}^{(+)}$ (%)	%$e_{ts}^{(-)}$ (%)	Set-point tracking	Load response
Simulation	0.0226	0.006	2.0	1.6	0.55	0.44	Suitable	Suitable
HIL	1.0800	0.300	1.1	2.1	0.30	0.58	Suitable	Suitable
Deviation	1.0570	0.294	−0.9	0.5	−0.25	0.14	N/A	N/A

V. CONCLUSION

This paper proposes the ACC with IMC and real-time frequency decoupling as a new control alternative for the applications of HESSs in parallel active topology. The validations performed in simulation and OPAL-RT suggest that the performance parameters obtained are good enough to use the controller in a custom prototype. Steady-state and transient errors show that the proposed controller performs better than the most commonly used controllers, especially when considering voltage disturbances in the controller. The results also suggest that the scalability of the system could allow the use of the controller in electric mobility applications.

References

[1] H. Farhangi, "The path of the smart grid," *IEEE Power and Energy Magazine*, vol. 8, no. 1, pp. 18-28, Jan. 2010.

[2] H. Gharavi and R. Ghafurian, "Smart grid: the electric energy system of the future [scanning the issue]," *Proceedings of the IEEE*, vol. 99, no. 6, pp. 917-921, Jun. 2011.

[3] J. A. Momoh, "Smart grid design for efficient and flexible power networks operation and control," in *Proceedings of 2009 IEEE PES Power Systems Conference and Exposition*, Seattle, WA, USA, Mar. 2009, pp. 1-8.

[4] R. H. Lasseter, "Microgrids," *in Proceedings of 2002 IEEE PES Winter Meeting Conference*, New York, USA, Jan. 2002, pp. 305-308.

[5] C. Schwaegerl and L. Tao, *The Microgrids Concept*. New York: John Wiley & Sons, 2013, pp. 1-24.

[6] C. Schwaegerl. (2009, Dec.). More microgrids: advanced architectures and control concepts for more microgrids. [Online]. Available: http://www.microgrids.eu/documents/668.pdf

[7] N. Hatziargyriou, N. Jenkins, G. Strbac *et al.*, "Microgrids–large scale integration of microgeneration to low voltage grids," in *Proceedings of CIGRE C6-309*, Paris, France, Aug. 2006, pp. 1-8.

[8] A. Narvaez, C. Cortes, and C. L. Trujillo, "Comparative analysis of topologies for the interconnection of batteries and supercapacitors in a hybrid energy storage system," in *Proceedings of IEEE 8th International Symposium on Power Electronics for Distributed Generation Systems (PEDG)*, Florianopolis, Brazil, Apr. 2017, pp. 1-6.

[9] T. S. Babu, K. R. Vasudevan, V. K. Ramachandaramurthy *et al.*, "A comprehensive review of hybrid energy storage systems: converter topologies, control strategies and future prospects," *IEEE Access*, vol. 8, pp. 148702-148721, Aug. 2020.

[10] R. A. Dougal, S. Liu, and R. E. White, "Power and life extension of battery-ultracapacitor hybrids," *IEEE Transactions on Components and Packaging Technologies*, vol. 25, no. 1, pp. 120-131, Aug. 2002.

[11] H. Kakigano, Y. Miura, and T. Ise, "Configuration and control of a dc microgrid for residential houses," in *Proceedings of 2009 Transmission Distribution Conference Exposition: Asia and Pacific*, Seoul, South Korea, Oct. 2009, pp. 1-4.

[12] A. Narvaez, C. Cortes, and C. Trujillo, "Real-time frequency-decoupling control for a hybrid energy storage system in an active parallel topology connected to a residential microgrid with intermittent generation," in *Applied Computer Sciences in Engineering*. Cham, Switzerland: Springer International Publishing, 2018, pp. 596-605.

[13] Y. Gu, W. Li, and X. He, "Frequency-coordinating virtual impedance for autonomous power management of DC microgrid," *IEEE Transactions on Power Electronics*, vol. 30, no. 4, pp. 2328-2337, Apr. 2015.

[14] Q. Xu, X. Hu, P. Wang *et al.*, "A decentralized dynamic power sharing strategy for hybrid energy storage system in autonomous DC microgrid," *IEEE Transactions on Industrial Electronics*, vol. 64, no. 7, pp. 5930-5941, Jul. 2017.

[15] M. Shi, X. Chen, J. Zhou *et al.*, "Advanced secondary voltage recovery control for multiple HESSs in a droop-controlled DC microgrid," *IEEE Transactions on Smart Grid*, vol. 10, no. 4, pp. 3828-3839, May 2018.

[16] P. Wang, X. Lu, W. Wang *et al.*, "Frequency division based coordinated control of three-port converter interfaced hybrid energy storage systems in autonomous DC microgrids," *IEEE Access*, vol. 6, pp. 25389-25398, Apr. 2018.

[17] Q. Xu, J. Xiao, X. Hu *et al.*, "A decentralized power management strategy for hybrid energy storage system with autonomous bus voltage restoration and state-of-charge recovery," *IEEE Transactions on Industrial Electronics*, vol. 64, no. 9, pp. 7098-7108, Oct. 2017.

[18] M. Morari, S. Skogestad, and D. F. Rivera, "Implications of internal model control for PID controllers," in *Proceedings of 1984 American Control Conference*, San Diego, USA, Jun. 1984, pp. 661-666.

[19] T. Kobaku, S. C. Patwardhan, and V. Agarwal, "Experimental evaluation of internal model control scheme on a DC-DC boost converter exhibiting nonminimum phase behavior," *IEEE Transactions on Power Electronics*, vol. 32, no. 11, pp. 8880-8891, Jan. 2017.

[20] U. Manandhar, A. Ukil, H. B. Gooi *et al.*, "Energy management and control for grid connected hybrid energy storage system under different operating modes," *IEEE Transactions on Smart Grid*, vol. 10, no. 2, pp. 1626-1636, Mar. 2019.

[21] S. Wen, S. Wang, G. Liu *et al.*, "Energy management and coordinated control strategy of PV/HESS AC microgrid during islanded operation," *IEEE Access*, vol. 7, pp. 4432-4441, Dec. 2019.

[22] A. Latorre, C. A. Cortes, and W. Martinez, "EMS for bidirectional boost converters of a hybrid energy storage system for residential microgrid applications," in *Proceedings of 2018 20th European Conference on Power Electronics and Applications*, Riga, Latvia, Sept. 2018, pp.1-9.

[23] D. Burmester, R. Rayudu, W. Seah *et al.*, "A review of nanogrid topologies and technologies," *Renewable and Sustainable Energy Reviews*, vol. 67, pp. 760-775, Jan. 2017

[24] Z. Kong, N. Cui, and P. Li, "Energy management strategy coordinating lithium-ion battery and ultra-capacitor for electric vehicle," in *Proceedings of 2017 36th Chinese Control Conference (CCC)*, Dalian, China, Jul. 2017, pp. 9291-9296.

[25] J. Cao and A. Emadi, "A new battery/ultracapacitor hybrid energy storage system for electric, hybrid, and plug-in hybrid electric vehicles," *IEEE Transactions on Power Electronics*, vol. 27, no. 1, pp. 122-132, Jan. 2012.

[26] A. Khaligh and Z. Li, "Battery, ultracapacitor, fuel cell, and hybrid energy storage systems for electric, hybrid electric, fuel cell, and plug-in hybrid electric vehicles: state of the art," *IEEE Transactions on Vehicular Technology*, vol. 59, no. 6, pp. 2806-2814, Aug. 2010.

[27] R. W. Erickson and D. Maksimovic, *Fundamentals of Power Electronics*. Boston: Springer, 2001, pp. 1-883.

[28] S. Bacha, I. Munteanu, and A. I. Bratcu, *Power Electronic Converters Modeling and Control: with Case Studies*. Berlin: Springer Science & Business Media, 2014, pp. 1-454.

[29] N. Mohan, *Power Electronics: Converters, Applications and Design*. New York: John Wiley & Sons, 2002, pp. 1-832.

[30] M. Korkmaz, O. Aydogdu, and H. Dogan, "Design and performance comparison of variable parameter nonlinear PID controller and genetic algorithm based PID controller," in *Proceedings of 2012 International Symposium on Innovations in Intelligent Systems and Applications*, Trabzon, Turkey, Jul. 2012, pp. 1-5.

[31] S. Lee and H. Almurib, "Control techniques for power converters in photovoltaic hybrid energy storage system," in *Proceedings of 3rd IET International Conference on Clean Energy and Technology (CEAT)*, Kuching, Malaysia, Nov. 2014, pp. 1-6.

[32] C. Edwards and S. Spurgeon, *Sliding Mode Control: Theory and Applications*. London: Taylor & Francis, 1998, pp. 1-237.

[33] C.-T. Chen, *Analog and Digital Control System Design: Transfer-Function, State-Space, and Algebraic Methods*. New York: Oxford University Press, 1995, pp. 1-600.

[34] E. Okyere, A. Bousbaine, G. T. Poyi *et al.*, "LQR controller design for quad-rotor helicopters," *The Journal of Engineering*, vol. 2019, no. 17, pp. 4003-4007, Jan. 2019.

[35] K. Zhou and J. C. Doyle, *Essentials of Robust Control*. Upper Saddle River, USA: Prentice-Hall, 1998, pp. 1-411.

[36] B. Francis and W. Wonham, "Internal model principle in control theory," *Automatica*, vol. 12, pp. 457-465, Sept. 1976.

[37] S. Bhattacharyya, A. Datta, and L. Keel, *Linear Control Theory: Structure, Robustness, and Optimization*. Boca Raton: CRC Press, 2018, pp. 1-924.

[38] Juwari, S. Chin, N. Samad *et al.*, "Two-degree-of-freedom internal model control for parallel cascade scheme," in *Proceedings of 2008 International Symposium on Information Technology*, Kuala Lumpur, Malaysia, Aug. 2008, pp. 1-6.

[39] A. Ghosh, M. Prakash, S. Pradhan *et al.*, "A comparison among PID, sliding mode and internal model control for a buck converter," in *Proceedings of IECON 2014-40th Annual Conference of the IEEE Industrial Electronics Society*, Dallas, USA, Oct. 2014, pp. 1001-1006.

[40] A. T. Azar and F. E. Serrano, "Robust IMC-PID tuning for cascade control systems with gain and phase margin specifications," *Neural Computing and Applications*, vol. 25, no. 5, pp. 983-995, Mar. 2014.

[41] A. Latorre, W. Martinez, and C. Cortes. (2021, Aug.). Hybrid energy storage systems controllers for island-mode considering disturbances. [Online]. Available: https://github.com/alatorre-UN/HESS island mode/tree/main

Alejandro Latorre received the B. Eng. degree in electronics engineering and the M. Eng. degree in industrial automation from Universidad Nacional de Colombia, Bogota, Colombia, in 2016 and 2021, respectively. He was a Graduate Visiting Scholar in the Electrical Engineering (ESAT) Department at KU Leuven-EnergyVille, Genk, Belgium, in 2008. He is currently working on his Ph.D degree at TU Delft, Delft, Netherlands. His current research interests include power converter control, hybrid energy storage systems, and energy storage systems in electrical mobility.

Wilmar Martinez received the M.Sc. degree in electrical engineering from

Universidad Nacional de Colombia, Bogota, Colombia, in 2013, and the Ph.D. degree in power electronics from Shimane University, Matsue, Japan, in 2016. He was a Commissioning Scientist at the Toyota Technological Institute, Nagoya, Japan, in 2016, and a Postdoctoral Researcher at Aalto University, Espoo, Finland in 2017. In 2018, he was a Visiting Researcher in the Power Electronic Systems (PES) group at ETH Zurich, Zurich, Switzerland. Since 2018, he has been an Assistant Professor in the Department of Electrical Engineering (ESAT) at KU Leuven-EnergyVille, Genk, Belgium. His current research interests include design automation of power converters, multi-domain modelling and validation of power components with emphasis on passives, and wide bandgap devices for electric mobility, renewable energy systems, and smart grids.

Camilo A. Cortes received the B. Eng. degree from Universidad Nacional de Colombia, Bogota, Colombia, in 2000 and the Ph.D. degree in Electrical Engineering (with honors) from Universidad Nacional de San Juan, San Juan, Argentina, in 2005. He was a Doctoral Visiting Student at FH Giessen-Friedberg and NLÖ, Hannover, Germany, in 2002, a Professor of Universidad de la Salle, Colombia, in 2005-2007, a Postdoctoral Visiting Scholar at KU Leuven, Belgium, in 2006, and a Visiting Researcher at the Galvin Center for Electricity Innovation, IIT, Chicago, USA, in 2015-2016. Since 2008, he is a Professor of Universidad Nacional de Colombia, Bogota, Colombia. He is a DAAD Research Ambassador since 2017 and Senior Member of IEEE. His current research interests include signal processing techniques, heuristic optimization, energy storage applications, microgrid planning, and modernization of power systems.